Nonlinear goniometry by second harmonic generation in AlGaAs nanoantennas

Luca Carletti,[1,§,] Giuseppe Marino,[2,3,4,§] Lavinia Ghirardini,[5,§] Valerio F. Gili,[2] Davide Rocco,[1] Ivan Favero,[2] Andrea Locatelli,[1] Anatoly V. Zayats,[4] Michele Celebrano,[5] Marco Finazzi,[5] Giuseppe Leo,[2] Costantino De Angelis,[1] and Dragomir N. Neshev [3]*

[1] Department of Information Engineering, Università degli Studi di Brescia, and INO-CNR, Via Branze 38, 25123 Brescia, Italy

[2] Matériaux et Phénomènes Quantiques, Université Paris Diderot—Sorbonne Paris Cité, CNRS UMR 7162, 10 rue A. Domon et L. Duquet, 75013 Paris, France

[3] Nonlinear Physics Centre, Research School of Physics and Engineering, the Australian National University, Canberra ACT 2601, Australia

[4] Department of Physics, King's College London, Strand, London WC2R 2LS, UK

[5] Department of Physics, Politecnico di Milano, Piazza Leonardo Da Vinci 32, 20133 Milano, Italy

ABSTRACT. High-permittivity semiconductor nanoresonators have shown a great potential for enhanced nonlinear light-matter interactions at the nanoscale due to the availability of a rich variety of resonances combined with low optical losses and a strong bulk nonlinearity. Second harmonic generation in AlGaAs nanoantennas can be extremely efficient and exhibits a complex radiation

pattern. However, the complexity of this radiation pattern, impose severe constrains on its practical applications and detection efficiency. In this work, we demonstrate, both experimentally and numerically, the control over the angular distribution of the second harmonic radiation pattern from a monolithic AlGaAs-on-AlOx nanodisk by varying the polarization and the angle of incidence of the pump beam. By tuning the angle of incidence from 0° to 45°, the detected second harmonic signal is monotonically increased up to over an order of magnitude thanks to the strong illumination dependence of the nonlinear radiation pattern when *s*-polarized light is employed. Our results demonstrate that precise angular measurements of the pump inclination can be performed with a sensitivity of up to 0.25 $(°)^{-1}$ and polarization discrimination, thus establishing a new technique for background-free nanoscale nonlinear goniometry.

INTRODUCTION.

Optical scattering from small particles is a phenomenon of paramount importance in many disciplines such as solid-state physics, meteorology, chemistry, biology, astronomy, and electrical engineering. Recent developments in nanophotonics demonstrated an impressive versatility in controlling different light properties (e.g., frequency, polarization, and directionality) through linear and nonlinear scattering from metallic or dielectric nanoparticles with resonances at optical wavelengths [1-7]. The use of resonant nanostructures made of semiconductor materials with a strong second or third-order nonlinear optical susceptibilities, such as Si and Geor GaP, AlGaAs and GaAs, respectively, provided a new paradigm for nonlinear nanophotonics [8-12]. For example, AlGaAs nanodisks resonators yield second harmonic generation (SHG) from near-infrared optical pump beams with unprecedented conversion efficiency up to about 0.1% [14-16]. This high efficiency

stems from the relatively high field enhancement factors achieved in the resonator volume and the high bulk nonlinearity of the nanoresonator material.

Furthermore, such dielectric resonators host a large variety of both electric and magnetic modes, allowing one to realize complex polarization[16, 17] and angular radiation patterns of the emitted second harmonic (SH) light[12, 18-21]. Such a richness of modes (or features) in the optical behavior can be potentially exploited to dynamically control the optical response [22, 23], which is a long-sought objective in the quest for the development of actively tunable nonlinear light sources. However, the symmetry of the nonlinear susceptibility tensor forbids SHG emission in the direction normal to the substrate for pump light using the common configuration with electric field in the plane with the substrate, thus reducing the collection efficiency with standard high-NA optics. It has been recently shown theoretically that this problem could be overcome by using a pump beam with a tilted incidence [18]. In such a configuration, the original doughnut radiation pattern [16] reshapes and one could obtain an SH beam propagating along the disk axis[12, 18]. Interestingly, this modification of the radiation pattern could allow measuring the angle of the pump with respect to the nanodisk axis, enabling a novel type of nonlinear goniometry with SHG from AlGaAs nanoantennas. However, implementation of such a nonlinear nanoscopic goniometry is still lacking.

Here we demonstrate such an approach to all-optical angular measurements as a practical application of nonlinear nanoscopic goniometry. This is achieved by exploring the variation of the SH radiation pattern from a single AlGaAs nanodisk as a function of the incidence direction and polarization of the pump beam. In our scheme, the change in the excitation beam angle is encoded first in the total SH signal measured by the detector and second into the relative SH emission between the normal and off-normal directions. Such background-free nanoscopic goniometer

allows for precision goniometry ranging from 0 to 45° and holds great potential if combined with super-resolution microscopy, adding the possibility to estimate a nanoparticle orientation. When combined with nanoscopic position sensors [24, 25], our scheme can provide a precise and reliable three-dimensional measurement of the position and orientation of light emitters relative to reference nanoparticles.

RESULTS AND DISCUSSION

We study the radiation pattern of SH light generated in single AlGaAs nanoantennas pumped at the magnetic dipole (MD) resonance. A schematic representation of the sample is shown in Fig. 1(a). It consists of a matrix of $Al_{0.18}Ga_{0.82}As$ nanodisks, with a nominal radius of 220 nm and height of 400 nm, grown on a 1-μm thick AlOx substrate (Fig. 1(b)). The 3-μm spacing between adjacent nanodisks in the array allows addressing individual elements in the array and makes near-field coupling between the elements negligible. The geometry of the nanoantenna is expected to exhibit a well pronounced MD resonance around 1.6 μm and a high-order multipole resonance at around 770 nm, as shown in Fig. 1(c) in the scattering efficiency spectra estimated by full-wave numerical simulations (see Methods). The radiation properties of second-harmonic light emitted in the backward direction are studied using a customized nonlinear microscopy setup (see Methods). The latter allows controlling the illumination angle by focusing the incident light rays off axis in the back focal plane (BFP) of a high numerical aperture (NA) objective, which also collects the SH radiation emitted from a single nanodisk in the backward direction. The SHG radiation pattern generated by the nanodisk, excited by a focused pump beam at a wavelength of 1570 nm, is recorded as a function of the angle of incidence, θ, defined as the angle between the disk axis and the wave vector direction of the pump beam (see Fig. 1(a)).

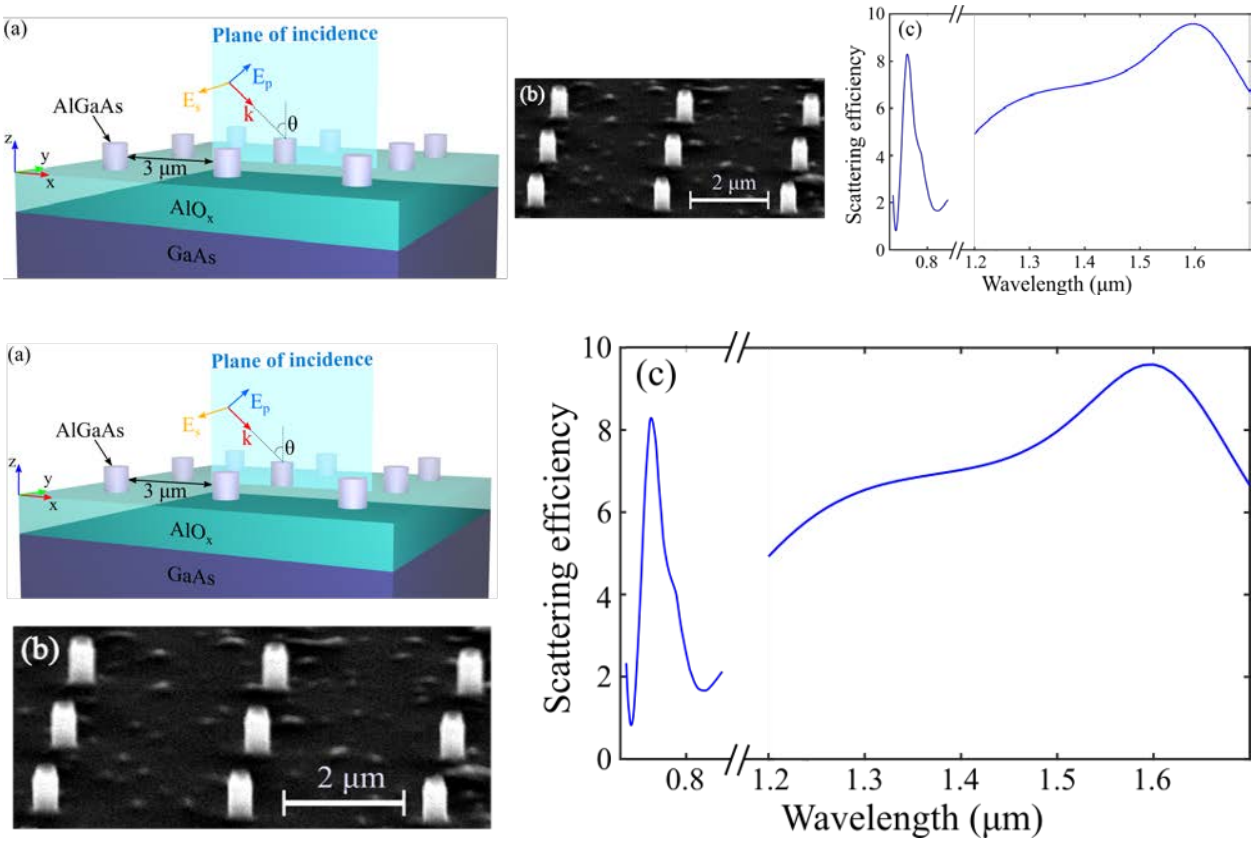

Figure 1. (a) Schematic representation of the fabricated AlGaAs-on-AlOx nanodisk array and the illumination geometry. The wavevector, *k*, and the electric field vectors for *s*, E_s, and *p*, E_p, polarizations on the plane of incidence are shown. (b) SEM image of the fabricated sample. (c) Total scattering efficiency spectrum of an AlGaAs nanoantenna calculated for a disk height of 400 nm and a radius of 220 nm on AlOx substrate.

Figures 2(a,c) show the BFP images of the backward SHG emission observed for either *s* or *p* polarization of the pump beam electric field. The incidence angle is varied from 0° to 45° (θ = 45° corresponds to the largest incidence angle of the pump beam that could be achieved with our experimental setup due to the finite NA of the focusing objective).

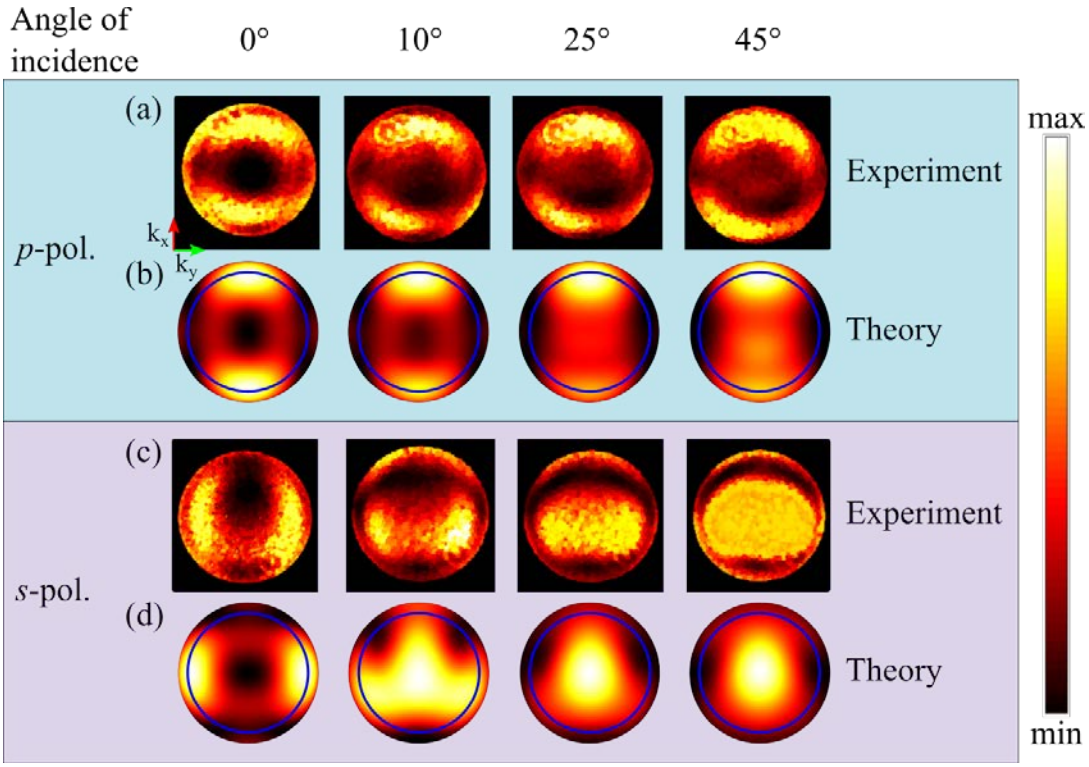

Figure 2. Back-focal plane images of the SH radiation emitted in the backward direction for different angles of incidence, θ, of light at the fundamental frequency for (a,b) *s*-polarized and (c,d) *p*-polarized excitation: (a,c) Experimental measurements and (b,d) numerical calculations. The blue circle in (b,d) represents the experimental NA = 0.85.

As it can be seen in Fig. 2(a,c), for a pump at normal incidence (θ = 0°), the SH light is radiated only at large angles, while no light is detected at the normal direction (the center of the BFP images), regardless of polarization. This feature has been observed in previous studies conducted on similar geometries and is related to the symmetry of the nonlinear susceptibility tensor and the excitation configuration [12, 16]. Since the AlGaAs nanodisk structure exhibits rotational symmetry around the *z*-axis, the in-plane and out-of-plane (*z*-axis) pump field components that are even and odd, respectively, for C2 rotations. For example, if we consider a linearly polarized plane wave propagating along the *z*-axis with an electric field parallel to the *x*-axis, we have that

$E_x(r,\varphi,z) = E_x(r,\varphi+\pi,z)$ and $E_z(r,\varphi,z) = -E_z(r,\varphi+\pi,z)$. The $\chi^{(2)}$ tensor of materials with zincblende lattices couples the in-plane and out-of-plane electric field components, so the generated SH field is proportional to the product $E_x \times E_z$, which is odd for C2 rotations. In this case, the propagation along the normal direction, which requires an in-plane component of the electric field being even with respect to C2 rotations, is forbidden. As we increase the angle of incidence θ of the pump beam, the behavior of the SH radiation changes. In the case of the *p*-polarized pump beam, the radiation pattern does not vary significantly as θ is increased up to 45°. In contrast, for the case of an *s*-polarized pump, we observe that for θ larger than 10° the SH radiation is redistributed. The emission lobes at large angles appear to merge in the lower side of the image into a single lobe along the normal direction (i.e., at the center of the BFP images). The intensity of this lobe increases with θ up to $\theta = 45°$. Thus, θ can be used as an adjustable parameter to shape the radiation profile of the SH generated by the AlGaAs nanodisk, as illustrated by the BFP images in Fig. 2(c).

To gain physical insight into the underlying phenomena, we analyzed the nonlinear optical response of the AlGaAs disk resonators using full-wave electromagnetic simulations (see Methods). The BFP images obtained experimentally (Fig. 2(a,c)) are compared with the numerical results (Fig. 2(b,d)). The measured SH radiation patterns well-agree with the calculated ones upon changing both pump polarization and angle of incidence. In particular, for *s*-polarized pump beam, we observe in both experiments and simulations a pronounced angular redistribution of the SH emission from two side lobes into a single central lobe. Simulations reproducing three-dimensional images of the backward radiation pattern for both *s* and *p* polarizations can be also found in the Supporting Information.

The angular redistribution is associated with a change of the total power detected by an observer in the backward direction. Figure 3(a) shows the SH collected power as a function of the angle of incidence of the fundamental beam, θ, for both of *s* and *p*-polarizations. The values estimated from the numerical simulations (solid lines) are superimposed with the experimental data (squares and diamonds), showing that the dependence of the SH detected power upon θ can be well reproduced by our model. Simulations for θ up to 60° can be found in the Supporting Information. The numerical results also show that the maximum SH collection efficiency is obtained for θ = 45°, which coincides with the maximum angle allowed by our oblique illumination microscopy setup. The discrepancy between the measurement and the numerical results could be attributed to possible differences between the nominal and the actual dimensions of the nanodisks or a small misalignment between the polarization of the pump electric field and the AlGaAs crystal axes. The latter could be due to various factors such as a tiny arch formed during the scan of the beam spot in the BFP (see Methods section), slightly leaning disks with respect to the substrate, or an unintentional few-degree offset of the crystal axes relative to the $[\bar{1}00]$ direction during the material growth [26].

From Fig. 3(a) we observe that, as θ changes from 0° to 45°, the increase of the collected SH power for the *s*-polarized pump beam is about 5 times larger than the one obtained for the *p* polarization. This feature highlights a strong sensitivity of the SHG on the variations of the pump polarization. In particular, for an *s*-polarized pump beam at θ = 45°, the SH power is enhanced by a factor of 10. Remarkably, this increase is monotonic with the angle θ. This is a unique feature, which can be exploited for the precise measurement of the angle between the pump-beam propagation direction and the disk axis, *i.e.* this structure can be considered a nanoscopic nonlinear goniometer. As seen in Fig. 3(a), in the range between 15° and 40°, the increase in the collected SH power is

linear. The coefficient of proportionality depends on the pump beam polarization and is equal to 1.6059×10^4 cts/° for *s*-polarization and 2.9165×10^3 cts/° for *p*-polarization. When these values are normalized to the SH power at $\theta = 15°$, we obtain a value of0.25 $(°)^{-1}$ for *s*-polarization and a value of $0.15(°)^{-1}$ for *p*-polarization.

The total SH efficiency, however, is not the most significant quantity to test the angular sensitivity at small angles. To evaluate the sensitivity at angles smaller than 15°, we exploit the spatial intensity distribution observed in the BFP images in Fig. 2(a,c). We define the normalized BFP intensity difference as $D_\theta = (I_a-I_b)/(I_a+I_b)$, where I_a and I_b are the measured intensity at one side, I_a, and at the center, I_b, of the radiation pattern captured in all the BFP images. D_θ represents an angle-dependent parameter, which is shown as a function of the angle of incidence, θ, and pump beam polarization in Fig. 3(b). The values of D_θ estimated from the experimental BFP images (squares and diamonds) are in excellent agreement with our simulations (continuous lines). Importantly, for angles between 0° and 10°, D_θ and θ have a linear relation with a slope of 0.087 $(°)^{-1}$ for *s*-polarization and 0.014 $(°)^{-1}$ for *p*-polarization.

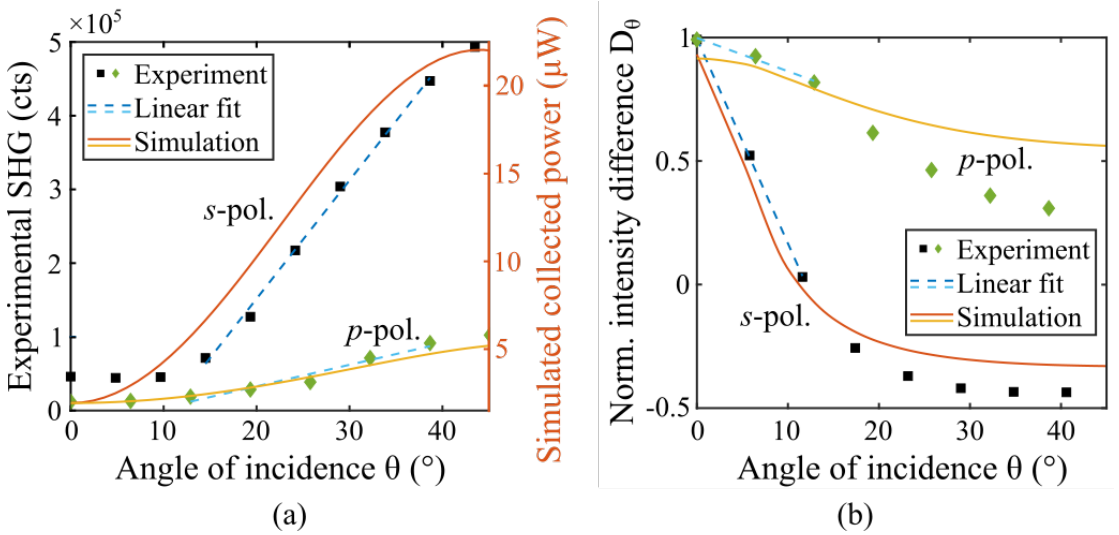

Figure 3. The angular dependences of (a) the collected SHG for the *s*- and *p*-polarized fundamental light and (b) normalized BFP intensity difference D_θ.

From the BFP images in Figure 2, we deduce that the polarization of the pump electric field plays a key role in determining the SH radiation pattern. Using our numerical framework, we perform a multipolar analysis of the linear and nonlinear scattering by the nanodisk to relate this behavior to the multipolar components (in Cartesian coordinates) excited in the nanodisk for the two pump polarizations. As shown in Figure 4(a), an *s*-polarized beam induces both an in-plane and out-of-plane MD moment at the pump frequency, as the angle θ increases. Due to the symmetry of the nonlinear susceptibility tensor of AlGaAs (see Methods), the nonlinear currents induced in the nanodisk by these electric fields at the SH frequency have a predominant *y*-axis component. As shown in Fig. 4(c) for $\theta = 45°$, such nonlinear currents exhibit an even-symmetry pattern that is compatible with a mode having an SH emission lobe in the normal direction. Furthermore, the enhancement of the SHG observed in Fig. 3(a) increases with the amplitude of the out-of-plane MD, which in turns increases monotonically with the angle of incidence. On the other hand, the multipolar analysis for *p*-polarized light, shown in Fig. 4(b), indicates that only an in-plane MD moment is excited, with nonlinearly generated currents at the SH frequency exhibiting odd symmetry in the *xy*-plane with respect to the *x*-axis when $\theta = 45°$ (see Fig. 4(d)). This current distribution is not compatible with the generation of SH light propagating along the nanocylinder axis, as the BFP images in Figs. 2(a,b) show. Thus, from the multipoles analysis we can conclude that the key phenomenon for the increase of the SHG in the normal direction is the excitation of an out-of-plane MD at the pump beam in addition to the in-plane MD. This effectively breaks the electric field symmetry inside the AlGaAs resonator and generates nonlinear currents at the SH

frequency that exhibit a symmetry that is compatible with disk modes radiating in the direction normal to the substrate.

To study the nature of resonant modes that redirect the SH emission, we further resort to the multipolar analysis of the electric field generated at the SH frequency. Figure 4(e) shows the efficiency related to each multipolar contribution at the SH frequency deduced from the distributions of the electric current density in the nanodisk that is generated by the *s*-polarized pump beam. At $\theta = 0°$, the SH radiation is dominated by an electric quadrupole that is characterized by radiation lobes at large angles and has a minimum along the normal axis. On the other hand, as θ increases to 45°, the electric dipole contribution starts to increase until it becomes the dominant one. In this case, the radiation pattern at the SH frequency is characterized by two main lobes pointing towards the forward and the backward directions along the disk axis. This normal SH emission effectively increases the collection efficiency and motivates the angular dependency observed in Fig. 3(a).

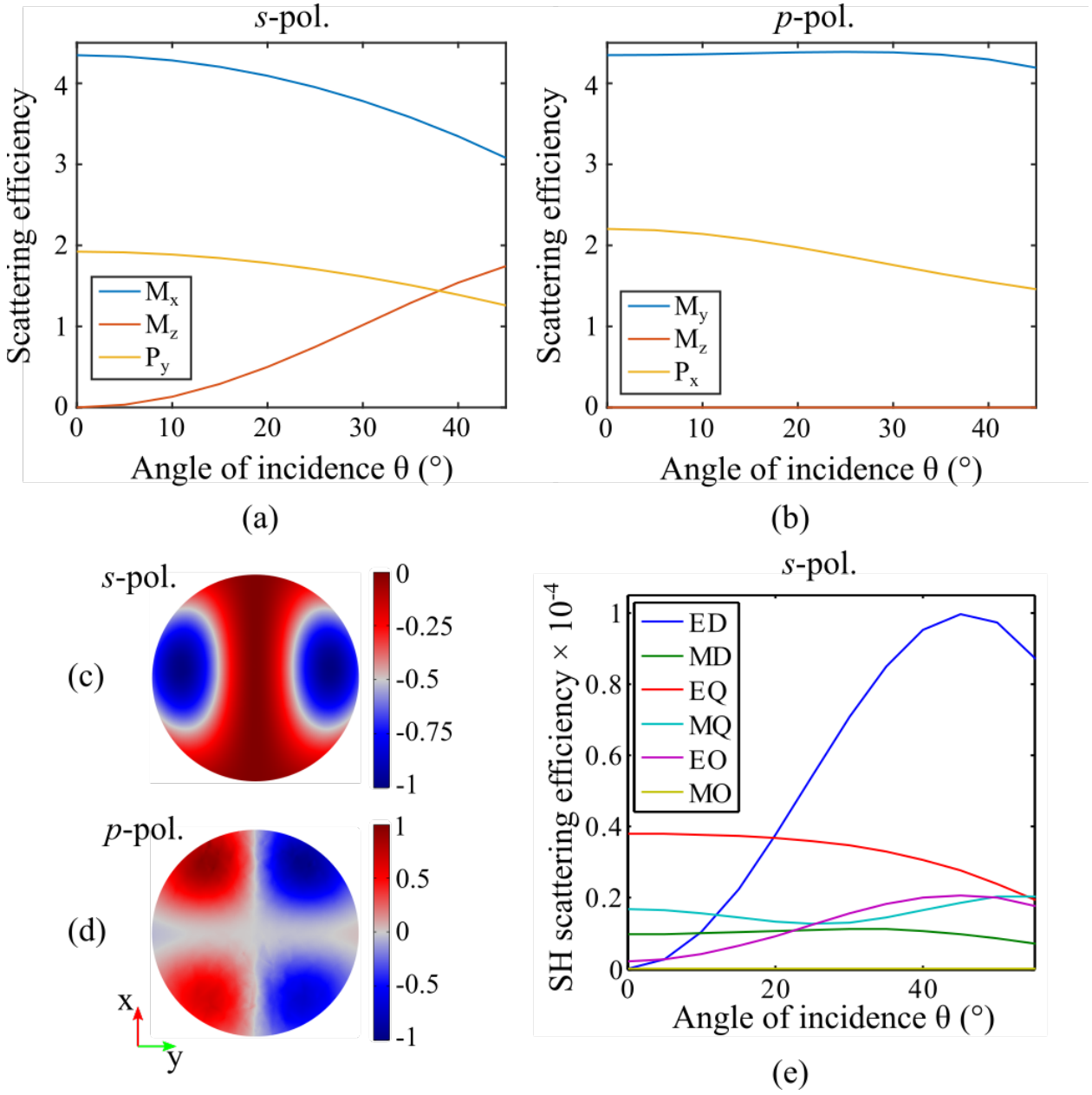

Figure 4. (a,b) The angular dependences of the linear scattering efficiency related to multipole components at the fundamental frequency for *s* and *p* polarizations (M_j with $j=x,y,z$ indicates the magnetic dipole oriented along the j-axis and P_x or P_y indicate the electric dipole along the x or y-axis). (c,d) The normalized y-component of the nonlinear currents induced by the pump beam at θ = 45° in the xy-plane in the middle of the nanodisk for (a) *s* and (b) *p* polarizations of the fundamental light. (e) The angular dependences of the total SH scattering related to multipole

components (the first letter indicates electric (E) or magnetic (M) multipole and the second letter indicates the type, i.e., dipole (D), quadrupole (Q), and octupole (O)).

CONCLUSIONS

We have demonstrated a precise angular measurement at the nanoscale using the polarization and angular dependences of the SH radiation from monolithic AlGaAs-on-AlOx nanodisks. Our results represent a novel approach for background-free all-optical goniometry. First, we employ the significant angle and polarization-dependent enhancement (up to an order of magnitude) of the total backward emitted SH power. Second, we exploit the differential change of the BFP intensity between the normal and oblique directions, due to the reshaping of the SH emission pattern. According to these two parallel approaches, our technique is capable of providing a high polarization and angular sensitivity of 0.087 $(°)^{-1}$ for angles from 0° to 10° and 0.25 $(°)^{-1}$ for angles from 15° to 40°. The full-vectorial simulations are in excellent agreement with our measurements and reveal that the observed effects are due to the selective excitation of different multipolar resonances in the nanodisk. These results illustrate the great potential of resonant nanostructures made of high-permittivity semiconductors to generate and manipulate light at the nanoscale.

METHODS

Simulations. Three-dimensional electromagnetic simulations were performed using the finite-element-method implemented in Comsol. We modeled isolated AlGaAs nanodisks on a semi-infinite low refractive index substrate using the geometrical parameters of the fabricated structures. Perfectly matched boundary conditions are used at the physical boundaries of the simulation to represent open boundaries. The dispersion of the permittivity of the disk nanoresonator material is

modeled by fitting analytical formulas to the experimental data [27]. The only non-vanishing components of the nonlinear susceptibility tensor of AlGaAs are the $\chi^{(2)}_{xyz}= \chi^{(2)}_{yzx}= \chi^{(2)}_{zxy}$, which are taken to be 100 pm/V. Their spectral dependence is neglected in the analyzed frequency range. The refractive indexes of air and substrate material are fixed to 1 and 1.6, respectively. To estimate the linear and nonlinear optical response of the nanodisks, we implemented a two-step procedure. In the first step, we calculate the linear optical response at the fundamental frequency by analyzing the scattering of the nanodisk upon a plane wave excitation with an intensity of 1 GW/cm^2. The scattering efficiency is calculated as $Q_{sca}=C_{sca}/\pi r^2$ where C_{sca} is the scattering cross-section and r is the disk radius. In the second step, the nonlinear optical response of the nanodisk at the SH frequency is calculated by using the nonlinear currents generated by the electric field at the fundamental frequency as a source. The multipolar coefficients of the mode at the SH frequency are calculated from the displacement current distribution inside the AlGaAs disk. This is defined as $\mathbf{J_s}(\mathbf{r}) = -i\omega_{SH}\varepsilon_0[\varepsilon_r(\mathbf{r})-1]\mathbf{E}(\mathbf{r})$, where $\mathbf{r}$ is the spatial position, ω_{SH} is the frequency, $\mathbf{E}$ is the electric field, and ε_r is the relative permittivity. To estimate the electric, a_E, and magnetic, a_M, coefficients of order (l,m) we follow the method described in Ref. [28]. To obtain the multipolar coefficients in a Cartesian coordinate system, we adopted the method described in Ref. [29].

Fabrication. Monolithic nanodisks are fabricated on the AlGaAs-on-aluminum-oxide material system [14]. A $[\bar{1}00]$ non-intentionally doped GaAs wafer, with a 400 nm layer of $Al_{0.18}Ga_{0.82}As$ on top of an aluminum-rich substrate was grown by molecular beam epitaxy. To improve the adhesion between the AlOx and the adjacent crystalline layers, the substrate consists of a 1-μm-thick $Al_{0.98}Ga_{0.02}As$ layer sandwiched between two 90-nm thick layers with linear tapers of Al molar fraction. The structures are defined by scanning electron microscope (SEM) lithography and dry etching with non-selective inductively coupled plasma-reactive-ion etching (ICP-RIE) plus

$SiCl_4$:Ar chemical treatment. The etching depth of 400 nm, controlled by a laser interferometer, defines the nanodisks and exposes the $Al_{0.98}Ga_{0.02}As$. Then, the etched sample is oxidized at 390 °C for 30 min in an oven equipped with in-situ optical monitoring, under a precisely controlled water vapor flow with N_2:H_2 gas carrier. After oxidation, each $Al_{0.18}Ga_{0.82}As$ nanodisk lies upon a uniform AlO_x substrate with a refractive index of about 1.6.

Experimental setup. The SHG from the AlGaAs nanodisks is characterized using a customized nonlinear microscope based on an ultrashort-pulse Er-doped fiber laser emitting at a central wavelength of 1570 nm with a pulse duration of 100 fs. To select the angle of incidence, the pump beam is focused by a long focal-length lens (f = 500 mm, mounted on a 3D translation stage) onto the BFP of a high NA air objective (Olympus, NA 0.85). In this configuration, by scanning the transverse position of the lens, we shift the beam position on the input aperture of the objective and therefore tune the angle of incidence from normal (beam at the center of the BFP) to 58° incidence (beam at the edge of the BFP). The measurements are performed in the 0°-45° angular range, since the latter is the maximum angle attainable before cutting-off the pump beam The radiation emitted from the sample is collected in epi-reflection through the same objective and filtered by a short-pass filter at 800 nm and a long-pass filter at 600 nm to remove any possible photoluminescence from the substrate and third harmonic emission component from the nanodisks, respectively. The SH emission is imaged on a cooled CCD camera in the real space, while the emission pattern in the Fourier space is studied by adding a confocal lens focusing on the objective BFP. The schematic of the setup can be found in the Supporting Information.

REFERENCES

1. Goncalves, M. R. Plasmonic nanoparticles: fabrication, simulation and experiments. *J Phys D Appl Phys* **2014,** 47, (21), 213001.

2. Kuznetsov, A. I.; Miroshnichenko, A. E.; Brongersma, M. L.; Kivshar, Y. S.; Luk'yanchuk, B. Optically resonant dielectric nanosctructures. *Science* **2016,** 354, (6314), aag2472.
3. Segovia, P.; Marino, G.; Krasavin, A. V.; Olivier, N.; Wurtz, G. A.; Belov, P. A.; Ginzburg, P.; Zayats, A. V. Hyperbolic metamaterial antenna for second-harmonic generation tomography. *Opt. Express* **2015**, 23, (24), 30730-30738.
4. Marino, G.; Segovia, P.; Krasavin, A. V.; Ginzburg, P.; Olivier, N.; Wurtz, G. A.; Zayats, A. V. Second-Harmonic Generation from Hyperbolic Plasmonic Nanorod Metamaterial Slab. *Laser & Photonics Reviews* **2018**, 12, (2), 1700189.
5. Li, G.; Sartorello, G.; Chen, S.; Nicholls, L. H.; Li, K. F.; Zentgraf, T.; Zhang, S.; Zayats, A. V. Spin and Geometric Phase Control Four-Wave Mixing from Metasurfaces. *Laser & Photonics Reviews* **2018**, 12, (6), 1800034.
6. Stefaniuk, T.; Olivier, N.; Belardini, A.; McPolin, C.; Sibilia, C.; Wronkowska, A. A.; Wronkowski, A.; Szoplik, T.; Zayats, A. V. Self-Assembled Silver–Germanium Nanolayer Metamaterial with the Enhanced Nonlinear Response. Advanced Optical Materials **2017**, 5, (22), 1700753.
7. Rocco, D.; Carletti, L.; Locatelli, L.; De Angelis, C. Controlling the directivity of all-dielectric nanoantennas excited by integrated quantum emitters. *J. of Opt. Soc. of Am. B* **2017**, 34, (9), 1918-1922
8. Shcherbakov, M. R.; Neshev, D. N.; Hopkins, B.; Shorokhov, A. S.; Staude, I.; Melik-Gaykazyan, E. V.; Decker, M.; Ezhov, A. A.; Miroshnichenko, A. E.; Brener, I.; Fedyanin, A. A.; Kivshar, Y. S. Enhanced Third-Harmonic Generation in Silicon Nanoparticles Driven by Magnetic Response. *Nano Lett* **2014,** 14, (11), 6488-92.
9. Smirnova, D.; Kivshar, Y. S. Multipolar nonlinear nanophotonics. *Optica* **2016,** 3, (11), 1241-1255.
10. Grinblat, G.; Li, Y.; Nielsen, M. P.; Oulton, R. F.; Maier, S. A. Enhanced Third Harmonic Generation in Single Germanium Nanodisks Excited at the Anapole Mode. *Nano Lett* **2016,** 16, (7), 4635-4640.
11. Cambiasso, J.; Grinblat, G.; Li, Y.; Rakovich, A.; Cortes, E.; Maier, S. A. Bridging the Gap between Dielectric Nanophotonics and the Visible Regime with Effectively Lossless Gallium Phosphide Antennas. *Nano Lett* **2017,** 17, (2), 1219-1225.
12. Carletti, L.; Rocco, D.; Locatelli, A.; De Angelis, C.; Gili, V. F.; Ravaro, M.; Favero, I.; Leo, G.; Finazzi, M.; Ghirardini, L.; Celebrano, M.; Marino, G.; Zayats, A. V. Controlling second-harmonic generation at the nanoscale with monolithic AlGaAs-on-AlOx antennas. *Nanotechnology* **2017,** 28, (11), 114005.
13. Timofeeva, M.; Lang, L.; Timpu, F.; Renaut, C.; Bouravleuv, A.; Shtrom, I.; Cirlin, G.; Grange R. Anapoles in Free-Standing III-V Nanodisks Enhancing Second-Harmonic Generation. *Nano Lett* **2018**, 18, (6), 3695-3702
14. Gili, V. F.; Carletti, L.; Locatelli, A.; Rocco, D.; Finazzi, M.; Ghirardini, L.; Favero, I.; Gomez, C.; Lemaitre, A.; Celebrano, M.; De Angelis, C.; Leo, G. Monolithic AlGaAs second-harmonic nanoantennas. *Opt Express* **2016,** 24, (14), 15965-71.
15. Liu, S.; Sinclair, M. B.; Saravi, S.; Keeler, G. A.; Yang, Y.; Reno, J.; Peake, G. M.; Setzpfandt, F.; Staude, I.; Pertsch, T.; Brener, I. Resonantly Enhanced Second-Harmonic Generation Using III–V Semiconductor All-Dielectric Metasurfaces. *Nano Letters* **2016,** 16, (9), 5426-5432.
16. Camacho-Morales, R.; Rahmani, M.; Kruk, S.; Wang, L.; Xu, L.; Smirnova, D. A.; Solntsev, A. S.; Miroshnichenko, A.; Tan, H. H.; Karouta, F.; Naureen, S.; Vora, K.; Carletti, L.;

De Angelis, C.; Jagadish, C.; Kivshar, Y. S.; Neshev, D. N. Nonlinear Generation of Vector Beams From AlGaAs Nanoantennas. *Nano Lett* **2016,** 16, (11), 7191-7197.
17. Ghirardini, L.; Carletti, L.; Gili, V.; Pellegrini, G.; Duo, L.; Finazzi, M.; Rocco, D.; Locatelli, A.; De Angelis, C.; Favero, I.; Ravaro, M.; Leo, G.; Lemaitre, A.; Celebrano, M. Polarization properties of second-harmonic generation in AlGaAs optical nanoantennas. *Opt Letters* **2017,** 42, (3), 559-562.
18. Carletti, L.; Locatelli, A.; Neshev, D.; Angelis, C. D. Shaping the Radiation Pattern of Second-Harmonic Generation from AlGaAs Dielectric Nanoantennas. *ACS Photonics* **2016,** 3, 1500-1507.
19. Timofeeva, M.; Bouravleuv, A.; Cirlin, G.; Shtrom, I.; Soshnikov, I.; Escalé, R. M.; Sergeyev, A.; Grange R. Polar Second-Harmonic Imaging to Resolve Pure and Mixed Crystal Phases along GaAs Nanowires. *Nano Letters* **2016,** *16*, (10), 6290-6297
20. Kruk, S. S.; Camacho-Morales, R.; Xu, L.; Rahmani, M.; Smirnova, D. A.; Wang, L.; Tan, H. H.; Jagadish, C.; Neshev, D. N.; Kivshar, Y. S. Nonlinear Optical Magnetism Revealed by Second-Harmonic Generation in Nanoantennas. *Nano Lett* **2017,** 17, (6), 3914-3918.
21. Guasoni, M.; Carletti, L.; Neshev, D.; De Angelis, C. Theoretical Model for Pattern Engineering of Harmonic Generation in All-Dielectric Nanoantennas. *IEEE J Quantum Elect* **2017,** 53, (3), 6100205.
22. Della Valle, G.; Hopkins, B.; Ganzer, L.; Stoll, T.; Rahmani, M.; Longhi, S.; Kivshar, Y. S.; De Angelis, C.; Neshev, D. N.; Cerullo, G. Nonlinear Anisotropic Dielectric Metasurfaces for Ultrafast Nanophotonics. *ACS Photonics* **2017,** 4, (9), 2129-2136.
23. Shcherbakov, M. R.; Liu, S.; Zubyuk, V. V.; Vaskin, A.; Vabishchevich, P. P.; Keeler, G.; Pertsch, T.; Dolgova, T. V.; Staude, I.; Brener, I.; Fedyanin, A. A. Ultrafast all-optical tuning of direct-gap semiconductor metasurfaces. *Nat Commun* **2017,** 8, (1), 17.
24. Liu, N.; Hentschel, M.; Weiss, T.; Alivisatos, A. P.; Giessen, H. Three-dimensional plasmon rulers. *Science* **2011,** 332, (6036), 1407-10.
25. Neugebauer, M.; Wozniak, P.; Bag, A.; Leuchs, G.; Banzer, P. Polarization-controlled directional scattering for nanoscopic position sensing. *Nat Commun* **2016,** 7, 11286.
26. Gili, V. F.; Carletti, L.; Chouchane, F.; Wang, G.; Ricolleau, C.; Rocco, D.; Lemaitre, A.; Favero, I.; Ghirardini, L.; Finazzi, M.; Celebrano, M.; De Angelis, C.; Leo, G. Role of the substrate in monolithic AlGaAs nonlinear nanoantennas. *Nanophotonics* **2018,** 7, (2), 517-521.
27. Gehrsitz, S.; Reinhart, F. K.; Gourgon, C.; Herres, N.; Vonlanthen, A.; Sigg, H. The refractive index of AlxGa1−xAs below the band gap: Accurate determination and empirical modeling. *Journal of Applied Physics* **2000,** 87, (11), 7825.
28. Grahn, P.; Shevchenko, A.; Kaivola, M. Electromagnetic multipole theory for optical nanomaterials. *New J of Phys* **2012,** 14, 093033.
29. Alaee, R.; Rockstuhl, C.; Fernandez-Corbaton, I. An electromagnetic multipole expansion beyond thelong-wavelength approximation. *Opt Commun* **2018,** 407, 17-21.

■ AUTHOR INFORMATION

Author Contributions

§ These authors contributed equally to this work.

■ ACKNOWLEDGMENTS

The paper and the participation of all the authors have been made possible in the framework of the Erasmus Mundus NANOPHI project, contract number 2013 5659/002-001. L.C., C.D.A., D.R. and A.L. acknowledge financial support from U.S. Army ("Engineering second order nonlinear effects in optical antennas") and CARIPLO ("SHAPES, Second-Harmonic Plasmon-Enhanced Sensing"). AZ acknowledges support from the ERC iPLASMM project, the Royal Society, and the Wolfson Foundation. G.M. and A.Z. acknowledge support from EPSRC (UK). G.L. acknowledges SATT IdF-Innov and SEAM Labex (PANAMA Project) for financial support. G.M.'s post-doc grant was funded by SEAM Labex (PANAMA Project) and MULTIPLY EU Co-fund program. V.F.G.'s grant was provided by the Double Culture - PhD program of Sorbonne Paris Cité. D.N.N. acknowledges the support of the Australian Research Council.